Ultrasensitive Detection of Aβ42 Seeds in Cerebrospinal Fluid with a Nanopipette-Based Real-Time Fast Amyloid Seeding and Translocation Assay

Nathan Meyer, Jeremy Bentin, Jean-Marc Janot, Imad Abrao-Nemeir, Saly Charles-Achille, Maud Pratlong, Alexis Aquilina, Eric Trinquet, Veronique Perrier, Fabien Picaud, et al.

Ultrasensitive detection of Aβ42 seeds in cerebrospinal fluid with a nanopipette-based RT-FAST assay

Nathan Meyer[1,2], Jeremy Bentin[3], Jean-Marc Janot[1], Imad Abrao-Nemeir[1], Saly Charles-Achille[1], Maud Pratlong[4], Alexis Aquilina[4], Eric Trinquet[4], Veronique Perrier[2], Fabien Picaud[3], Joan Torrent[2§], Sebastien Balme[1§*]*

[1] Institut Européen des Membranes, UMR5635 UM ENCSM CNRS, Place Eugène Bataillon, 34095 Montpellier cedex 5, France.

[2] INM UM, CNRS, INSERM, Place Eugène Bataillon, 34095 Montpellier cedex 5, France.

[3] Laboratoire de Nanomédecine, Imagerie et Thérapeutique, EA4662, Université Bourgogne-Franche-Comté (UFR Sciences et Techniques), Centre Hospitalier Universitaire de Besançon, 16 route de Gray, 25030 Besançon, France

[4]PerkinElmer, Parc Marcel Boiteux, 30200 Codolet, France

§ Equal contribution

* Corresponding authors : sebastien.balme@umontpellier.fr and Joan.torrent@inserm.fr

ABSTRACT

In this work, early-stage Aβ42 aggregates were detected using a real-time Fast Amyloid Seeding and Translocation (RT-FAST) assay. Specifically, Aβ42 monomers were incubated in buffer solution with and without preformed Aβ42 seeds in a quartz nanopipette coated with L-DOPA. Then, formed Aβ42 aggregates were analysed on flyby resistive pulse sensing at various incubation time points. Aβ42 aggregates were detected only in the sample with Aβ42 seeds after 180 minutes of incubation, giving an on/off readout of the presence of preformed seeds. Moreover, this RT-FAST assay could detect preformed seeds spiked in 4% cerebrospinal fluid/buffer solution. However, in this condition, the time to detect the aggregates and the nanopipette lifetime were increased. Analysis of Cy3-labelled Aβ42 monomer adsorption on a quartz substrate after L-DOPA coating by confocal fluorescence spectroscopy and molecular dynamic simulation showed the huge influence of Aβ42 adsorption on the aggregation process.

Keywords: Amyloid, Nanopore, single molecule, Alzheimer Disease, diagnosis

INTRODUCTION

The prevalence of Alzheimer's disease (AD) is steadily increasing worldwide (50 million cases in 2019) due to the longer life expectancy [1]. This global epidemic raises serious concerns due to the lack of effective treatments [2]. Early diagnosis might allow delaying AD clinical symptoms, reducing hospitalization in favour of home care, and decreasing the direct and indirect costs for the society. However, the main difficulty in developing a reliable early diagnostic assay for AD is related to the intrinsic disordered properties of β-amyloid (Aβ) peptides, the deposition of which is a major AD feature. The high energetically state of the monomer peptide promotes its self-assembly to gain energetic stability[3]. Moreover, Aβ misfolded peptides can convert naturally unfolded peptides, and thus make them pro-aggregative following a prion-like mechanism[4]. Over time, Aβ peptide aggregation leads to the formation of structures rich in β-sheets (called amyloid fibrils) that display various sizes, morphologies and biochemical properties (Supplementary Figure 1). Before reaching the amyloid fibril structure, many transient species are formed, including oligomers and protofibrils organized in β-sheet structures[5,6]. Oligomers formed at an early stage seem to be strongly involved in AD development. These structures are considered the most toxic and are the first amyloid intermediates before the formation of protofibrils and fibrils [7]. Interestingly, it was estimated that only 10% of spontaneously formed oligomers evolve to fibrils [8]. This means that most oligomers are dissociated to react again and form new amyloidogenic oligomers, through primary or secondary nucleation processes.

Much research effort has focused on strategies to detect early-stage Aβ aggregates directly in cerebrospinal fluid (CSF) or blood [9]. However, the low concentration of low-

molecular Aβ oligomers, their transient state, and their polymorphism complicate the design of a specific and sensitive assay. Previous studies have shown that antibody-based assays, such as ELISA, western blotting, single-molecule arrays[11,10] and immunosensors[12], induce a bias because the oligomer species polymorphism, especially at an early stage of aggregation, could influence the interaction with the antibody. On the other hand, a protein seed amplification assay (called Real Time Quaking – Induced Conversion, or RT-QuIC) relies on the self-propagation mechanism in which misfolded prion proteins (i.e. the seeds) convert the normal unfolded prion proteins into the misfolded form that is included in the growing assembly[13,14]. This assay is now adapted for AD (using the tau aggregates as biomarker) and synucleinopathies (using the Parkinson's disease-associated α-synuclein form)[15,16]. Conversely, the use of Aβ42 seeds as a biomarker for AD was tested only once, and the results have not been replicated yet[17].

Single-molecule nanopore sensing is another promising technology to characterize amyloid without any labelling[18]. Several types of artificial nanopores created on polymers by track-etching[19], on silicon nitride by ion/electron beam etching[20], or obtained from quartz pipette pulling (i.e. nanopipettes)[21] have been tested. Then, amyloid is detected by resistive pulse sensing (RPS) in which a ionic current readout is obtained by applying a constant voltage across the nanopore[22,23]. The amyloid passage through the nanopore induces a current perturbation characterized by changes in amplitude ($\Delta I/I$) and duration (Δt) that depend on the intrinsic properties of the protein assembly, such as size, charge and diffusion coefficient[25,24]. The nanopore-based sensing approach might allow discriminating among several amyloid populations in the same sample when their sizes are in the same range as the nanopore diameter[26]. The simplicity of nanopore tuning and

functionalization allows adapting them for detecting small oligomers and up to protofibrils, as demonstrated for lysozyme[27], β-lactoglobulin[28], Aβ[29,30,32,31], α-synuclein[35,34,33] and tau[36]. These studies have two common points: i) nanopores were functionalized to prevent fouling; and ii) amyloid samples were tested at various incubation times that corresponded to different aggregation steps. Recently, our group has carried out a proof-of-concept study showing that the nanopipette-based Real Time-Fast Amyloid Seeding and Translocation (RT-FAST) assay can be used to detect preformed α-synuclein seeds[37]. In this assay, preformed α-synuclein seeds are added to a quartz nanopipette reservoir (reaction chamber) that contains an excess of recombinant α-synuclein. Addition of α-synuclein seeds induces the misfolding and aggregation of recombinant α-synuclein monomers into amyloid that is detected at the tip side of the nanopipette with an adjustable pore diameter (nanopore) by resistive pulse sensing. Preformed α-synuclein seeds generated a positive signal consisting of larger and more abundant current blockades, thus providing a fast, binary (yes/no) readout of their presence. We then hypothesized that the RT-FAST assay could be adapted to detect preformed Aβ peptide seeds because the detection is based on the aggregate volume and not structure. Indeed, compared with α-synuclein, Aβ aggregation follows more complex pathways and most oligomers do not reach the β-sheet aggregate stage (Figure 1)[38]. This is likely the main barrier to the development of an efficient, reproducible and reliable assay for Aβ aggregate detection. Here, we demonstrated that our RT-FAST assay can detect preformed Aβ peptide seeds in buffer solution and also in buffer solution with 4% CSF, thus overcoming this barrier. Specifically, we first produced Aβ peptide seeds and functionalized nanopipettes. Then, we performed the RT-FAST assay to detect preformed seeds in the buffer and for the first time in CSF. By analysing the obtained

signals, we calculated the volume of the detected aggregates using a geometrical model. To go further than our previous work, we also investigated experimentally and by molecular dynamic simulation whether Aβ adsorption played an important role in the aggregation process and in pipette fouling.

RESULTS AND DISCUSSION

Seed production and characterization.

To ensure the experimental reproducibility, we purified Aβ42 monomers by fast protein liquid chromatography (FPLC). This step is crucial because during the solubilization step, Aβ42 assemblies are formed and co-exist with monomers (Figure 1a) and can contribute to the formation of preformed seeds and to the RT-FAST assay results (we used the same procedure also for Cy3-labelled monomers – supplementary Figure 2a). We carried out the in vitro production of preformed seeds at 25 °C at a concentration of 30 μM (equivalent monomer). We monitored the aggregation kinetics using the fluorescence of thioflavin T (ThT) that revealed the β-sheet structure of protofibrils and fibrils. Aβ aggregation follows basically three steps: i) lag phase when ThT fluorescence signal remains low, ii) exponential phase when the β-sheet structure grows, and iii) plateau when the fibrils are formed (Figure 1b – supplementary Figure 2b). We focused on the beginning of the exponential phase (end of the lag phase) that in our experimental setup occurred after 5 days of incubation. At this stage, the sample was composed of polymorphic aggregates and small fibrillar structures (see transmission electron microscopy, TEM, images, Figure 1c-e). However, ThT fluorescence signal was ~6 times lower than what observed in the plateau phase when amyloid fibrils are formed. Therefore, β-sheet fibrils are sparsely populated at this stage. As kinetic monitoring of fibril formation using ThT fluorescence is not suitable

for early-stage oligomer detection, we chose this stage (beginning of the exponential phase/end of the lag phase) to collect preformed seeds for detection using the RT-FAST assay. Moreover, oligomeric amyloid species are the most toxic for neurons, strengthening the interests to detect them early. To ensure that the selected preformed seeds could accelerate aggregation, we added them to Aβ42 monomers (4 μM), in 96-well plates, and monitored ThT fluorescence signal over time. In the presence of preformed seeds (8 nM equivalent monomer), aggregation started after 30 minutes of incubation, whereas in their absence the lag phase was longer (~80 min). This confirmed the seeding properties of the selected Aβ42 species present at an early time during fibril development. The time scale (minutes) to reach fibril formation was faster in plates than in tubes. This is due to the larger surface-to-volume ratio of wells that also promotes aggregation[39]. Then, we repeated this experiment using the low preformed seed (0.2 nM) and monomer (100 nM) concentrations typically used for RT-FAST assays. In these conditions, not enough β-sheets or mature fibrils were formed to be detected by ThT fluorescence (Supplementary Figure 2b).

Pipette characterization.

The RT-FAST assay require a nanopipette that is composed of two parts: the reservoir and the nanopore. All nanopipettes used in this work (Supplementary Table 1) were pulled following the same program. To improve reproducibility, we selected only the nanopipettes that displayed similar conductance. Scanning electron microscopy (SEM) analysis of a set of nanopipettes showed that they had a diameter of ~32 nm±2 nm and an angle of ~11°±1° (Figure 1f-h and Supplementary Figure 3). We functionalized each nanopipette with L-dopamine (L-DOPA) to limit the nanopore area fouling. L-DOPA functionalization also

reduced the contact angle of a water drop on a quartz substrate (same conditions of coating as for the nanopipette) from ~51° to ~40° (inset Figure 1i and Supplementary Figure 3). We could expect to obtain a more hydrophilic surface although we did not activate the quartz surface. To confirm L-DOPA presence inside the nanopore, we recorded the current-voltage (IV) responses of all used nanopipettes in 1M NaCl/1x PBS pH7.4 before and after functionalization (Figure 1i and Supplementary Figure 3i). The current rectification observed on the IV curves (due to the presence of negative charges on the quartz surface) was more pronounced after L-DOPA functionalization following the increase of the surface charge induced by the amine and carboxylate moieties. This suggested partial functionalization of the nanopipette surface.

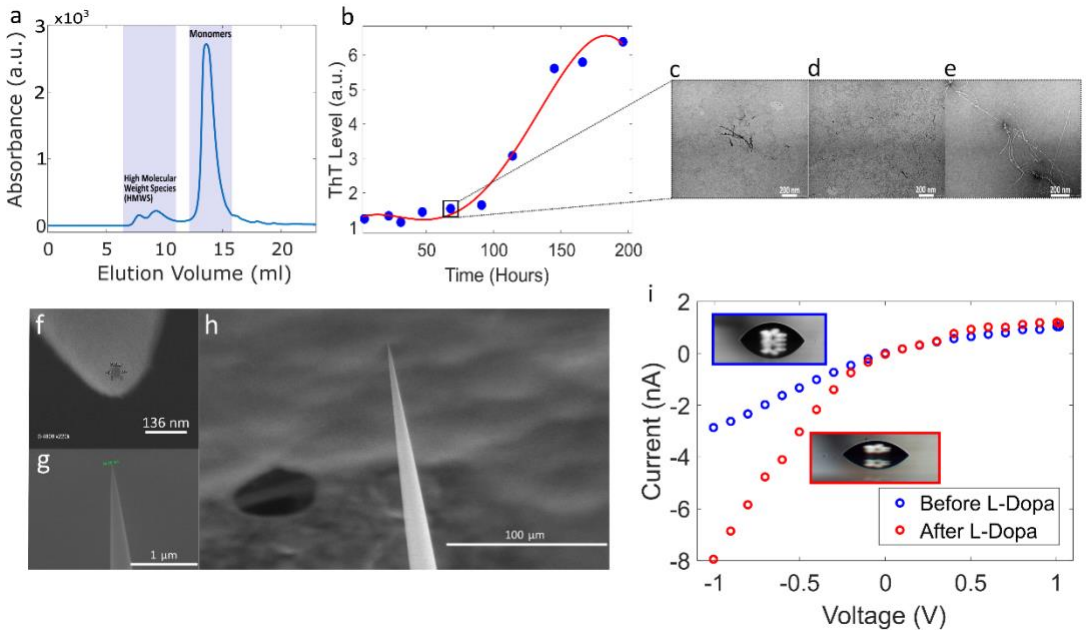

Figure 1: a) Size exclusion chromatogram of β 1-42 peptides after solubilization. Only the peak corresponding to the monomer fraction was harvested, frozen in liquid nitrogen, and stored at -80 °C until the RT-FAST experiments. b) Aβ42 aggregation kinetics at 25 °C

(30 µM equivalent monomers) in a tube followed by ThT fluorescence quantification. c, d, e) Transmission electronic microscopy analysis of the morphology of seeds collected after 5 days of incubation, and used for the RT-FAST experiments (the scale bar represent 200 nm). f, g, h) Scanning electron microscopy images showing the pipette tip, shank and overall geometry, respectively. i) IV curve of a nanopipette before (blue) and after coating (red) with L-DOPA (pipette n. 4). Insets show the contact angle with the quartz surface before (blue) and after (red) L-DOPA coating in the same conditions used for the nanopipettes. The left angle and right angles for the condition without L-DOPA coating are 51.16° and 51.18°, respectively. The left angle and right angles for the condition with L-DOPA coating are 37.49° and 41.99 °.

RT-FAST assay to detect preformed seeds in buffer solution

The RT-FAST assay is based on the ability of preformed α-synuclein seeds to accelerate aggregation[37]. To demonstrate the method transferability to Aβ42 peptides, we performed experiments using two pipette sets: one for the control condition (i.e. 100 nM of Aβ monomers alone) and the other for the experimental condition (i.e. 100 nM of Aβ monomers and 0.2 nM, equivalent monomer, of preformed seeds). We applied a constant voltage of -500 mV in the pipette reservoir for 10 minutes followed by 20 minute break for each cycle, for a total time of 300 minutes (Figure 2a). In the control condition, we did not record any significant event (i.e. current blockade) in three independent experiments (pipettes n° 1, 2, 3) (Figure 2b, blue traces). This indicated that no aggregate was formed during this time, or that spontaneously formed aggregates were too small and/or not abundant enough to be detected by the nanopore. Conversely, in the experimental condition (six independent experiments, pipettes n° 4, 5, 6, 7, 8, 9), we observed events after 120-

150 min (Figure 2b, red traces). This indicated that the seeded newly formed aggregates were larger than those formed in the control condition. This gives a simple and efficient on/off readout of the presence of preformed seeds. Event frequency in the six independent experiments increased from 120 min to 210 min and then decreased (Figure 2c). Three hypotheses can explain this bell-shaped curve. First, the nanopore geometry is optimal to detect objects smaller than its pore diameter. Therefore, when aggregates become larger than the nanopore, they cannot be detected any longer. Second, the capture rate is in function of the aggregate diffusion coefficient and concentration. Indeed, the aggregation process should have two outcomes: i) increasing the aggregate size (and thus slowing the diffusion coefficient), and ii) decreasing the aggregate concentration. These outcomes may explain why the capture rate decreases after some time. Third, the bell-shaped curve could be explained by the nanopipette fouling over time that modifies its diameter and thus progressively reduces the newly formed aggregate detection efficiency. This last hypothesis is the most plausible because we observed a baseline current drift after 300 min. Then, we analysed the relative amplitudes of the current blockade ($\Delta I/I$) and event duration (Δt) for all independent samples that contained preformed seeds (Figure 2d, g, j, e, h, k; Supplementary Figure 4). Regardless of the incubation time, the dwell time ranged between 1 and 100 ms, in good agreement with literature data on the detection of protein aggregates by nanopipettes[41,40,32]. The $\Delta I/I$ values varied between 2 and 8%, showing the detected species polymorphism; however, it did not increase over time. This shows that the detected seeds did not grow during the experiment. We also estimated the volume of the detected aggregates (V_{amy}) using a geometrical model previously proposed for conical nanopores[26] (See Extending data 5: Model to determine the amyloid volume and supplementary Figure

5). The calculation using the nanopore diameter and angle range determined by SEM showed $\Delta I/I$ values between 0.02 to 0.08, which corresponded to aggregates with a volume between 500 and 2000 nm^2 (Figure 2m, f, i, l). We plotted the mean volume deduced from the $\Delta I/I_0$ distribution centre at each time point and using the mean nanopipette geometry deduced from SEM data (a=11° r_t=34 nm and L_p=22 µm). For all experiments, the volume of detected aggregates fluctuated over time and did not increase. This may seem counterintuitive because the aggregate size during amyloid formation should increase over time. However, similar observations were reported previously for α-synuclein (RT-FAST)[37] and Aβ42 samples collected during the lag phase[29]. These previous findings were explained by the fact that during the lag phase, most aggregates do not directly form fibrils. Indeed, aggregation follows an association/dissociation scheme to adopt a rather energetically stable state. This provides a highly heterogenous sample composed of transient species[38,42]. To confirm the presence of transient species during the lag phase, we followed the spontaneous Aβ42 aggregation (Figure 4o) by Fluorescence Resonance Energy Transfer-Homogeneous Time-Resolved Fluorescence (FRET-HTRF). The results obtained for Aβ42, and confirmed for Aβ40 (Extended Data 6: Additional FRET experiments with Aβ40 and Supplementary Figure 6), showed that the HTRF signal oscillated when ThT fluorescence signal was at baseline. When the ThT fluorescence signal increased, the HTRF signal gradually decreased due to aggregation. This means that transient oligomers, without structured β-sheets, are present during the lag phase. The lack of correlation between fluorescence-based approaches and the oscillation profile obtained by FRET-HTRF is in good agreement with the RT-FAST results. Indeed, the ThT signal detected in plates at the concentration used for RT-FAST did not reveal any β-sheet

structure. This emphasizes that the RT-FAST assay is suitable to detect oligomers at an earlier stage than the ThT assay.

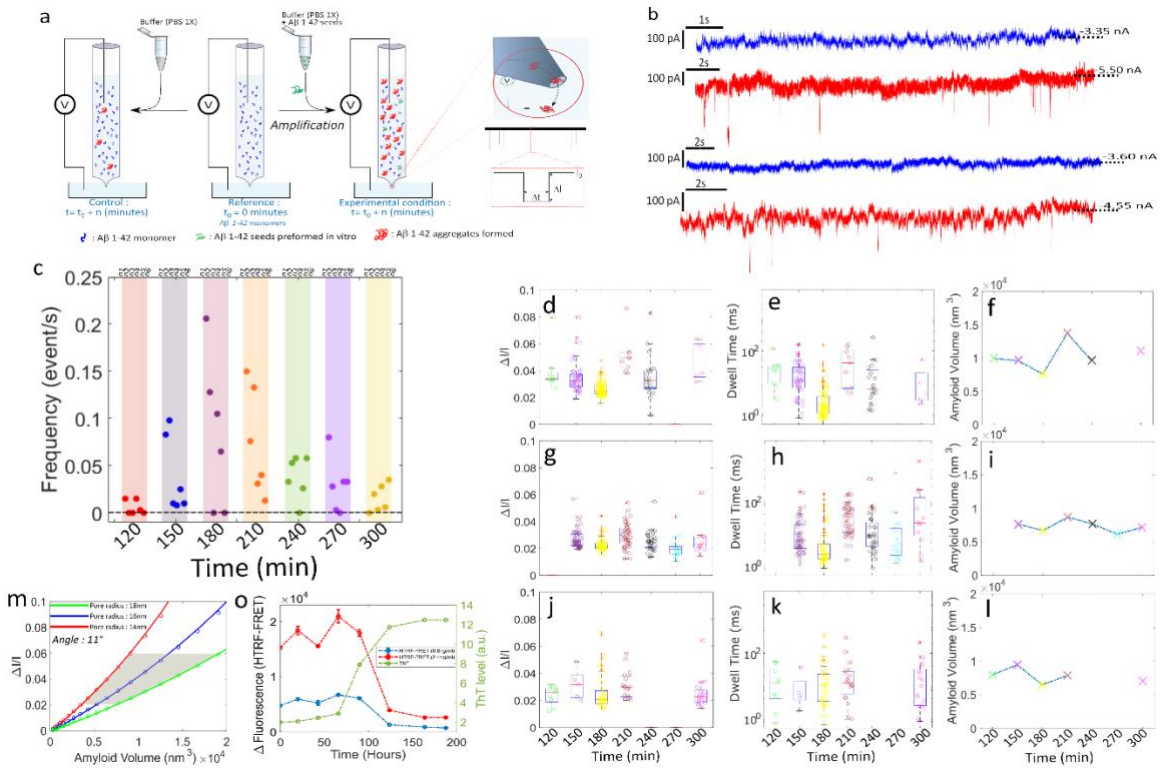

Figure 2: a) Schematic representation of the principle to detect AD biomarkers by RT-FAST. Aβ 1-42 monomer aggregation is faster in the presence (right panel) than in the absence (left panel) of preformed seeds. Therefore, compared with the pipette without seeds, the pipette with seeds will contain many more aggregates that will be detected by the nanopipette. b) Current traces for the control condition (without seeds) after 180 minutes of aggregation (blue, pipettes n. 2, top, and n.1, bottom) and for the experimental condition with seeds (red, pipettes n. 8, top, and n.6, bottom). Note the working electrode is placed inside the nanopipette. c) Current blockade frequency detected at different aggregation times recorded in six individual experiments with seeds (pipettes n. 4,5,6,7,8,

and 9). d, g, j) ΔI/I of the current blockade obtained for the pipettes containing seeds (n. 4,5, and 6, respectively). e, h, k) Dwell time of the current blockade for the pipettes containing seeds (n. 4,5, and 6, respectively). f, i, l) Volume of amyloid aggregates passing through the nanopipette estimated with a geometrical model based on the amplitude (DI/I) of the pipette blockage (pipettes n. 4,5, and 6, respectively). m) Graphical resolution of the model to estimate the amyloid volume passing into the nanopipette based on the current blockade amplitude. Volumes were estimated for several pore radii (14 nm, 16 nm and 18 nm shown in red, blue and green, respectively). The volume estimation was done for an opening angle of 11°. o) Aβ42 aggregation kinetics monitored by ThT fluorescence (green curve). FRET-HTRF fluorescence signal shows oscillations of species during the early phases of aggregation (lag phase) at two concentrations: 0.8 ng/ml (blue) and 2.4 ng/ml (red).

Adsorption of Aβ42 monomers on a quartz substrate.

To understand the nanopipette surface impact, we analysed the adsorption of Cy3-labelled Aβ42 monomers (100 nM) on a quartz substrate after L-DOPA coating by confocal fluorescence spectroscopy (Figure 3a)[44,43]. This method allows the direct measurement of the interfacial concentration changes of Aβ42-Cy3 monomers. Cy3 fluorescence lifetime did not show any significant change when measured in solution and after adsorption on the substrate. This suggests that the chromophore is not in direct contact with the substrate. Thus, we can reasonably assume that adsorption is due to the peptide chain. The adsorption kinetics (Figure 3b and Supplementary Figure 7) showed an increase in the interfacial concentration of Aβ42 for 400 s - 500 s that reached a plateau of ~17000 Aβ42-Cy3 monomer molecules/μm^2. From the measured interfacial concentration, we could calculate

the adsorption constant and thus correct the real monomer concentration in the nanopipette (see Extended Data 7: Aβ adsorption kinetics). As the kinetic constant was 0.215, the adsorption would reduce the concentration from 100 nM to 78.5 nM at equilibrium. A more detailed analysis of interfacial concentration fluctuations suggested a non-homogeneous protein distribution, in good agreement with the partial L-DOPA functionalization suggested by the contact angle measurements.

To confirm the true Aβ42 affinity for the surface, we performed molecular dynamic simulation on quartz surfaces with three L-DOPA grafting rates, from 0% to 50%, on the surface, in several initial conditions (absolute Aβ42 position and orientation relative to the quartz surface), and for a sufficient long simulation time (at least 100 ns). We plotted pair interaction changes for the Aβ-quartz, Aβ-L-DOPA, and Aβ-solvent, compared with the absolute value when Aβ was free in the solvent (Figure 2 c-e; Extended Data 8 Molecular dynamic simulations and Supplementary Figure 8). The results of simulation showed that for the three conditions, Aβ42 was adsorbed slightly and reversibly on the quartz surface, confirming our experimental hypothesis. We also found that it was also slightly attracted by L-DOPA molecules (negative pair interaction). However, the interaction with the solvent showed the most important modification that almost counterbalanced the effects due to the quartz surface and L-DOPA.

Further analyses of the simulation data indicated that direct interactions between Aβ and the quartz surface are not necessarily favourable. Indeed, only few residues that fluctuates during the simulation were involved in interactions with the quartz. These results can be explained by the low lateral diffusion coefficient of structured water molecule and ion layers on the interface with the quartz surface (compared with bulk ones). In addition, the

bulk reservoir creates a strong thermal agitation (pair interaction between Aβ and bulk water) at -2000 kcal/mol, while the possible link between one residue and the surface fluctuates at -50 to 50 kcal/mol. Thus, the good binding Aβ42/surface association is sometimes difficult to reach due to strong perturbations of the water diffusion in the bulk and on the surface. L-DOPA presence on the quartz surface modified the adsorbed solvent structure by leaving several ions in the bulk water. When its concentration increased, the coordination number of water with the functionalized groups decreased (Supplementary Figure 9), as previously reported [45]. The pair interaction between the Aβ42 and L-DOPA also was interesting because it could compensate for the losses due to water disruption. Consequently, Aβ42 adsorption on the surface was slightly favoured. These simulations highlighted a weak and reversible adsorption of Aβ42 on the quartz surface, becoming more favourable with the L-DOPA coating.

Then, before testing the RT-FAST assay with CSF-containing medium, we evaluated CSF effect on Aβ-Cy3 adsorption because CSF protein composition could compete or cooperate with Aβ42-Cy3. The adsorption kinetics in the presence of 4% CSF showed an interfacial concentration of ~6000 molecules/μm^2 at equilibrium (Figure 4b and Supplementary Figure 6). Moreover, the affinity constant (0.067) was lower than in buffer alone (0.215). This adsorption decrease can be attributed to albumin, which is the main CSF protein (60% to 80% of all CSF proteins) and competes with Aβ42-Cy3 adsorption on the surface defects.

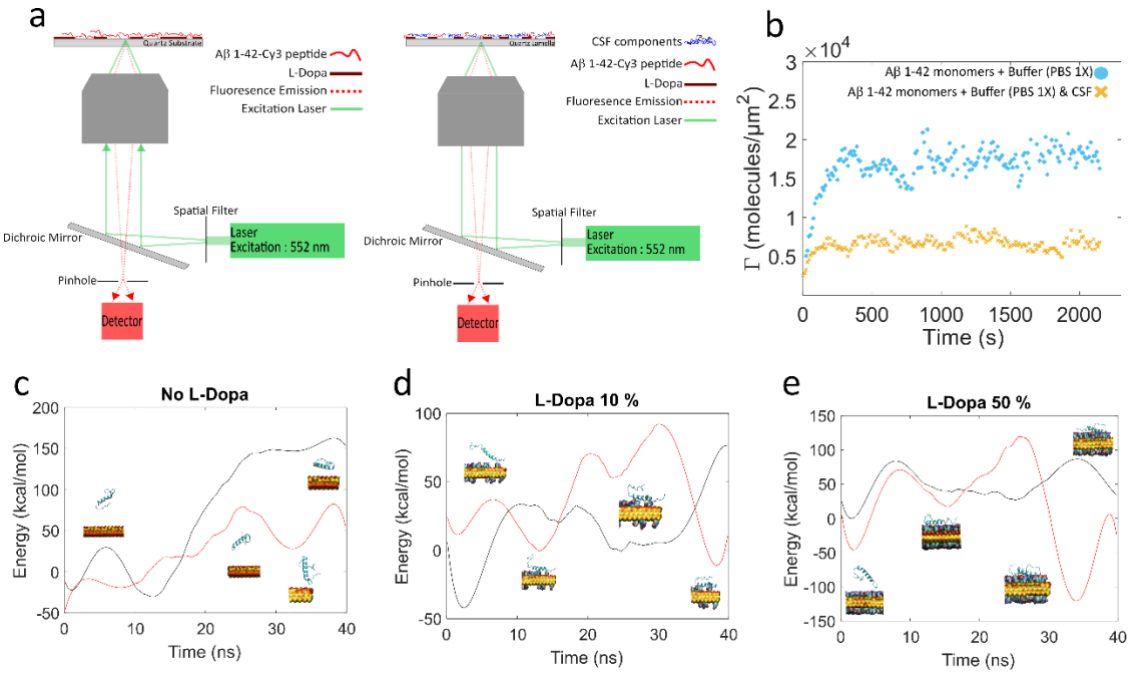

Figure 3: a) Schematic representation of the confocal spectrometer to record the Aβ-Cy3 absorption kinetics on a quartz substrate in the absence (left) and presence (right) of 4% CSF. b) Aβ-Cy3 absorption on the quartz substrate in buffer without (blue) and with 4% CSF (orange). c-e) Rescaled total pair energy interaction between Aβ and its neighbours (water, ions, quartz), with different L-DOPA coverage percentages (note: E = 0 is for the total pair interaction obtained in pure solvent). The large energy fluctuations indicate the simulation times when Aβ is adsorbed on the surface. Due to the increase of L-DOPA on the surface, the global pair interaction of Aβ decreases slightly, and the adsorption stability progressively increases. Each component of these total pair interactions is depicted in Supplementary Figure 7. Red and black curves are for two different simulation conditions.

RT-FAST assay to detect preformed seeds in CSF artificially spiked and diluted in buffer.

We performed RT-FAST assays in buffer with 4% CSF, as commonly done for the RT-QuIC assay (Figure 4a). CSF presence did not induce any significant current perturbation.

Indeed, albumin volume (~82 nm^3) should induce a relative current blockage of ~0.02% according to equation 1. This value is too low to be distinguished from noise. On the other hand, CSF presence made the nanopipettes more stable, as indicated by the absence of significant current drift after 300 min. We then performed RT-FAST assays with control solution (100 nM of Aβ42 monomers in 4% CSF) and experimental solution (100 nM of Aβ42 monomers and 0.2 nM of Aβ42 preformed seeds in 4% CSF). The adsorption constant measured by confocal spectroscopy indicated that the corrected monomer concentration was 93 nM (~15% more than what found using buffer alone). As before, we did not detect any event in the control solution (Figure 4b). With the experimental solution, we observed the first events after 210 min. This was longer than for the assays performed without CSF. The frequency increased with the aggregation time in the pipette (the frequency of events in three independent experiments is shown in Figure 4c). The delay in observing a sufficiently large event could be explained by several factors. First, the presence of proteins in CSF, such as transthyretin. This protein binds to Aβ42 and could inhibit the aggregation process [46,40]. Second, the decrease in Aβ42 adsorption constant, observed by confocal fluorescence, might slow down the aggregation kinetics. Indeed, one of the hypotheses to explain the aggregation acceleration in RT-FAST is based on the idea that the adsorption of monomers on the surface is favoured by a high surface-to-volume ratio. This is confirmed by the faster aggregation time of experiments done in plates compared with tubes[39]. At this stage, we could not determine which effect is predominant. However, from a practical point of view, the longer time required to detect Aβ42 aggregates was counterbalanced by a longer pipette lifetime, likely due to the decrease of Aβ42 adsorption. Then, we calculated the $\Delta I/I$ and Δt of events obtained using independent

triplicates (experimental solution containing preformed seeds). The *ΔI/I* varied between 2 and 20% and was larger than that recorded in buffer, highlighting a more heterogeneous sample composition (Figure 4d, g, j). Regardless of the time (between 180 min and 390 min), the dwell times were between 1 and 100 ms (Figure 7e, h, k), as observed for experiments performed with buffer alone. Using Eq. 1, the amyloid aggregate volumes ranged between 700 and 2500 nm^3 (Figure 7f, i, l), and were larger than those observed in buffer. Therefore, we concluded that the RT-FAST assay detected the transient oligomeric species populated during the lag phase. The most interesting result was that CSF addition did not interfere with the recorded signal because most of CSF protein components are too small and too weakly concentrated to be differentiated from the noise (Supplementary Figure 10). Thus, the RT-FAST assay can be used also to test CSF samples.

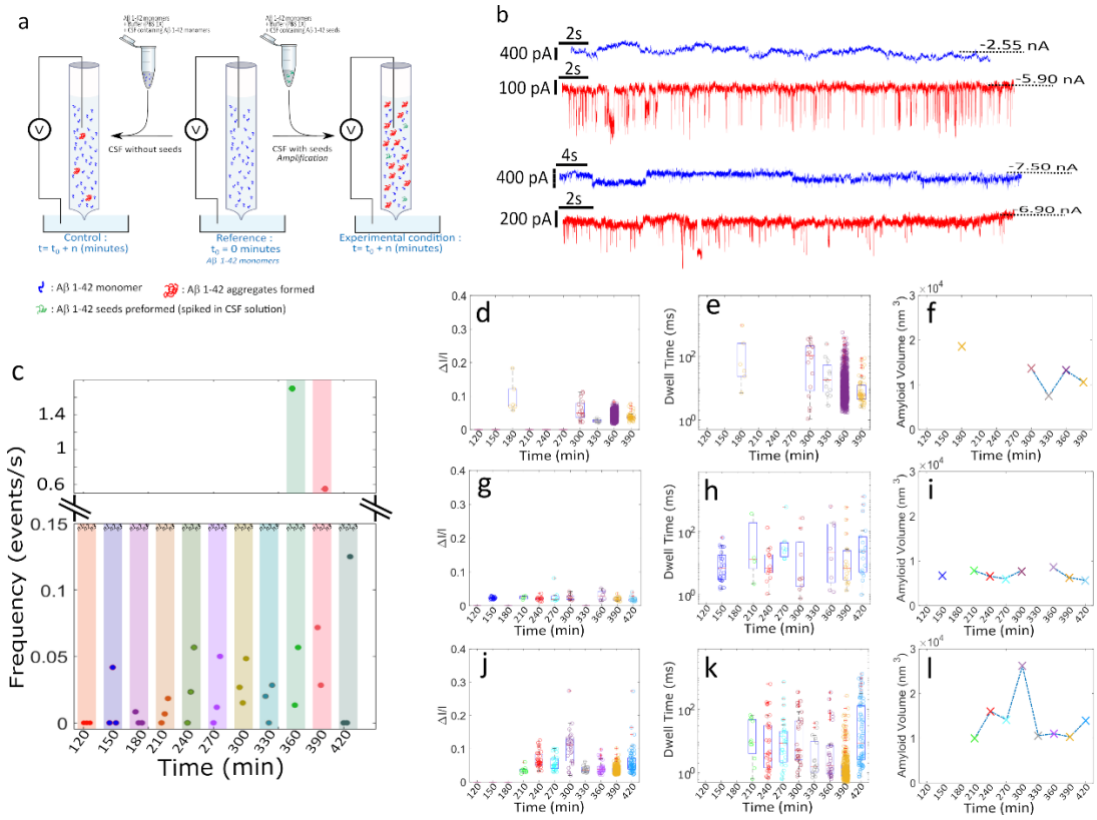

Figure 4: a) Schematic representation of the principle of detection of Aβ42 in buffer with 4% CSF. b) Current traces in the control condition after 390 minutes of incubation (blue; pipette n. 10 top, and pipette n. 12, bottom) and in the experimental condition (red; pipette n. 13 top, and pipette n. 12, bottom). c) Current blockade frequency detected at different aggregation time points in the pipettes n. 13, 14 and 15 (n=3 independent experiments). d, g, j) ΔI/I of the current blockade obtained for the seed-containing pipettes n. 13, 14, and 15, respectively. e, h, k) Dwell times of the current blockade for the seed-containing pipettes n. 13, 14, and 15, respectively. f, i, l) Amyloid aggregate volume estimated with a geometrical model based on the current blockade amplitude (ΔI/I) for the seed-containing pipettes n. 13, 14, and 15, respectively.

CONCLUSION

Here, we showed that our RT-FAST assay can be used also to detect aggregation promoted by preformed Aβ42 seeds. The assay is based on protein misfolding amplification. Nanopores allows the detection of small transient oligomers during the lag phase. The positive signal easily establishes the presence of preformed seeds. Moreover, we demonstrated that the RT-FAST assay is suitable to detect preformed seeds spiked in 4% CSF in buffer. Importantly, the RT-FAST assay allows detecting the presence of preformed seeds at an early stage of the aggregation process, before the formation of β-sheet structures, and requires a low concentration of monomers. Therefore, the RT-FAST assay is fast and requires less consumables, enabling its optimization for a real diagnostic tool. Our results also highlight the huge influence of Aβ adsorption on the aggregation process. These data may help to design an analytical method for amyloid detection, and

may partly explain the experimental variability often observed with Aβ42. In addition, the combined results of the RT-FAST and HTRF assays confirmed the aggregate polymorphism and transient properties during the lag phase.

In view of the challenge to develop a suitable assay for Aβ42 aggregate detection in biofluids, the RT-FAST assay holds great promise to indirectly detect amyloids in patients' biofluids. In addition, RT-FAST is a powerful method to study protein aggregation, including the impact of therapeutic inhibitors, and may lead to advances in drug design to treat AD.

Acknowledgments

This work was founded by Agence Nationale de la Recherche (ANR-19-CE42-0006, NanoOligo).

Supporting information: Material and Methods, Scheme of amyloid growth, Characterization of aβ 1-42-Cy3 peptides and Aggregation kinetics, Characterisation of Nanopipettes, Additional results of RT-FAST assay performed in buffer, Model to determine the amyloid volume, Additional FRET experiments with Aβ40, Aβ adsorption kinetics, Molecular dynamic simulations, Comparison of RT-fast experiment without and with 4% CSF

References

(1) Alzheimer's Disease International. *World Alzheimer report 2019: attitudes to dementia.*, 2019.

(2) Vaz, M.; Silvestre, S. *European journal of pharmacology* **2020**, DOI: 10.1016/j.ejphar.2020.173554.

(3) Meersman, F.; Dobson, C. M.; Heremans, K. *Chemical Society reviews* **2006**, DOI: 10.1039/B517761H.

(4) Willbold, D.; Strodel, B.; Schröder, G. F.; Hoyer, W.; Heise, H. *Chemical reviews* **2021**, DOI: 10.1021/acs.chemrev.1c00196.

(5) Arosio, P.; Knowles, T. P. J.; Linse, S. *Physical chemistry chemical physics : PCCP* **2015**, DOI: 10.1039/c4cp05563b.

(6) Knowles, T. P. J.; Vendruscolo, M.; Dobson, C. M. *Nature reviews. Molecular cell biology* **2014**, DOI: 10.1038/nrm3810.

(7) Haass, C.; Selkoe, D. J. *Nature reviews. Molecular cell biology* **2007**, DOI: 10.1038/nrm2101.

(8) Michaels, T. C. T.; Šarić, A.; Curk, S.; Bernfur, K.; Arosio, P.; Meisl, G.; Dear, A. J.; Cohen, S. I. A.; Dobson, C. M.; Vendruscolo, M.; Linse, S.; Knowles, T. P. J. *Nature chemistry* **2020**, DOI: 10.1038/s41557-020-0452-1.

(9) Kulenkampff, K.; Wolf Perez, A.-M.; Sormanni, P.; Habchi, J.; Vendruscolo, M. *Nat Rev Chem* **2021**, DOI: 10.1038/s41570-021-00254-9.

(10) Hong, W.; Wang, Z.; Liu, W.; O'Malley, T. T.; Jin, M.; Willem, M.; Haass, C.; Frosch, M. P.; Walsh, D. M. *Acta neuropathologica* **2018**, DOI: 10.1007/s00401-018-1846-7.

(11) Hölttä, M.; Hansson, O.; Andreasson, U.; Hertze, J.; Minthon, L.; Nägga, K.; Andreasen, N.; Zetterberg, H.; Blennow, K. *PloS one* **2013**, DOI: 10.1371/journal.pone.0066381.

(12) Aprile, F. A.; Sormanni, P.; Perni, M.; Arosio, P.; Linse, S.; Knowles, T. P. J.; Dobson, C. M.; Vendruscolo, M. *Science advances* **2017**, DOI: 10.1126/sciadv.1700488.

(13) Green, A. J. E. *Practical neurology* **2019**, DOI: 10.1136/practneurol-2018-001935.

(14) Saborio, G. P.; Permanne, B.; Soto, C. *nature* **2001**, DOI: 10.1038/35081095.

(15) Groveman, B. R.; Orrù, C. D.; Hughson, A. G.; Raymond, L. D.; Zanusso, G.; Ghetti, B.; Campbell, K. J.; Safar, J.; Galasko, D.; Caughey, B. *Acta neuropathologica communications* **2018**, DOI: 10.1186/s40478-018-0508-2.

(16) Metrick, M. A.; Ferreira, N. d. C.; Saijo, E.; Kraus, A.; Newell, K.; Zanusso, G.; Vendruscolo, M.; Ghetti, B.; Caughey, B. *Acta neuropathologica communications* **2020**, DOI: 10.1186/s40478-020-0887-z.

(17) Salvadores, N.; Shahnawaz, M.; Scarpini, E.; Tagliavini, F.; Soto, C. *Cell reports* **2014**, DOI: 10.1016/j.celrep.2014.02.031.

(18) Houghtaling, J.; List, J.; Mayer, M. *SMALL* **2018**, DOI: 10.1002/smll.201802412.

(19) Ma, T.; Janot, J.-M.; Balme, S. *Small Methods* **2020**, DOI: 10.1002/smtd.202000366.

(20) Xue, L.; Yamazaki, H.; Ren, R.; Wanunu, M.; Ivanov, A. P.; Edel, J. B. *Nat Rev Mater* **2020**, DOI: 10.1038/s41578-020-0229-6.

(21) Stanley, J.; Pourmand, N. *APL Materials* **2020**, DOI: 10.1063/5.0020011.

(22) Bayley, H.; Martin, C. R. *Chemical reviews* **2000**, DOI: 10.1021/cr980099g.

(23) Meyer, N.; Abrao-Nemeir, I.; Janot, J.-M.; Torrent, J.; Lepoitevin, M.; Balme, S. *Advances in colloid and interface science* **2021**, DOI: 10.1016/j.cis.2021.102561.

(24) Yusko, E. C.; Johnson, J. M.; Majd, S.; Prangkio, P.; Rollings, R. C.; Li, J.; Yang, J.; Mayer, M. *NATURE NANOTECHNOLOGY* **2011**, DOI: 10.1038/nnano.2011.12.

(25) Carlsen, A.; Tabard-Cossa, V. *Proteomics* **2022**, DOI: 10.1002/pmic.202100068.

(26) Giamblanco, N.; Coglitore, D.; Gubbiotti, A.; Ma, T.; Balanzat, E.; Janot, J.-M.; Chinappi, M.; Balme, S. *ANALYTICAL CHEMISTRY* **2018**, DOI: 10.1021/acs.analchem.8b03523.

(27) Giamblanco, N.; Coglitore, D.; Janot, J.-M.; Coulon, P. E.; Charlot, B.; Balme, S. *Sensors and Actuators B: Chemical* **2018**, DOI: 10.1016/j.snb.2018.01.094.

(28) Giamblanco, N.; Janot, J.-M.; Gubbiotti, A.; Chinappi, M.; Balme, S. *Small Methods* **2020**, DOI: 10.1002/smtd.201900703.

(29) Meyer, N.; Arroyo, N.; Baldelli, M.; Coquart, N.; Janot, J. M.; Perrier, V.; Chinappi, M.; Picaud, F.; Torrent, J.; Balme, S. *Chemosphere* **2021**, DOI: 10.1016/j.chemosphere.2021.132733.

(30) Meyer, N.; Arroyo, N.; Janot, J.-M.; Lepoitevin, M.; Stevenson, A.; Nemeir, I. A.; Perrier, V.; Bougard, D.; Belondrade, M.; Cot, D.; Bentin, J.; Picaud, F.; Torrent, J.; Balme, S. *ACS sensors* **2021**, DOI: 10.1021/acssensors.1c01523.

(31) Yusko, E. C.; Prangkio, P.; Sept, D.; Rollings, R. C.; Li, J.; Mayer, M. *ACS NANO* **2012**, DOI: 10.1021/nn300542q.

(32) Yu, R.-J.; Lu, S.-M.; Xu, S.-W.; Li, Y.-J.; Xu, Q.; Ying, Y.-L.; Long, Y.-T. *CHEMICAL SCIENCE* **2019**, DOI: 10.1039/c9sc03260f.

(33) Li, X.; Tong, X.; Lu, W.; Yu, D.; Diao, J.; Zhao, Q. *NANOSCALE* **2019**, DOI: 10.1039/c9nr00023b.

(34) Hu, R.; Diao, J.; Li, J.; Tang, Z.; Li, X.; Leitz, J.; Long, J.; Liu, J.; Yu, D.; Zhao, Q. *Scientific reports* **2016**, DOI: 10.1038/srep20776.

(35) Chau, C. C.; Radford, S. E.; Hewitt, E. W.; Actis, P. *Nano Lett.* **2020**, DOI: 10.1021/acs.nanolett.0c02246.

(36) Giamblanco, N.; Fichou, Y.; Janot, J.-M.; Balanzat, E.; Han, S.; Balme, S. *ACS sensors* **2020**, DOI: 10.1021/acssensors.0c00193.

(37) Meyer, N.; Janot, J.-M.; Torrent, J.; Balme, S. *ACS central science* **2022**, DOI: 10.1021/acscentsci.1c01404.

(38) Dear, A. J.; Meisl, G.; Šarić, A.; Michaels, T. C. T.; Kjaergaard, M.; Linse, S.; Knowles, T. P. J. *CHEMICAL SCIENCE* **2020**, DOI: 10.1039/c9sc06501f.

(39) Toprakcioglu, Z.; Kamada, A.; Michaels, T.; Xie, M.; Krausser, J.; Wei, J.; Saric, A.; Vendruscolo, M.; Knowles, T. *Adsorption Free Energy Predicts Amyloid Protein Nucleation Rates*, 2022.

(40) Li, W.; Bell, N. A. W.; Hernández-Ainsa, S.; Thacker, V. V.; Thackray, A. M.; Bujdoso, R.; Keyser, U. F. *ACS NANO* **2013**, DOI: 10.1021/nn4004567.

(41) Kubánková, M.; Lin, X.; Albrecht, T.; Edel, J. B.; Kuimova, M. K. *ANALYTICAL CHEMISTRY* **2019**, DOI: 10.1021/acs.analchem.9b01221.

(42) Dear, A. J.; Michaels, T. C. T.; Knowles, T. P. J.; Mahadevan, L. *The Journal of chemical physics* **2021**, DOI: 10.1063/5.0055925.

(43) Balme, S.; Janot, J.-M.; Déjardin, P.; Vasina, E. N.; Seta, P. *Journal of Membrane Science* **2006**, DOI: 10.1016/j.memsci.2006.07.034.

(44) Balme, S.; Coulon, P. E.; Lepoitevin, M.; Charlot, B.; Yandrapalli, N.; Favard, C.; Muriaux, D.; Bechelany, M.; Janot, J.-M. *Langmuir : the ACS journal of surfaces and colloids* **2016**, DOI: 10.1021/acs.langmuir.6b02048.

(45) Zhou, M.; Cheng, K.; Jia, G. *Journal of Molecular Liquids* **2017**, DOI: 10.1016/j.molliq.2016.11.079.

(46) Costa, R.; Gonçalves, A.; Saraiva, M. J.; Cardoso, I. *FEBS letters* **2008**, DOI: 10.1016/j.febslet.2008.02.034.

TABLE OF CONTENT

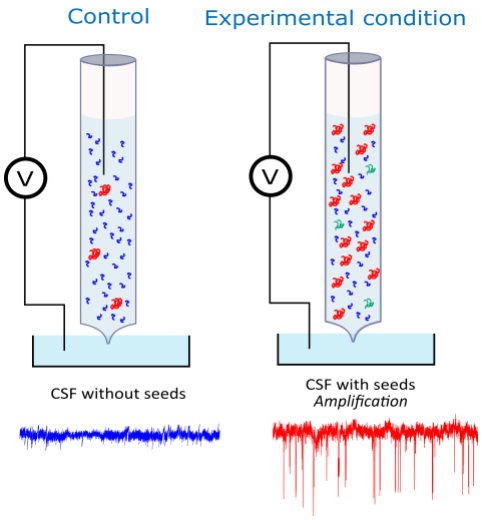

Ultrasensitive detection of Aβ42 seeds in cerebrospinal fluid with a nanopipette-based RT-FAST assay

Nathan Meyer[1,2], Jeremy Bentin[3], Jean-Marc Janot[1], Imad Abrao-Nemeir[1], Saly Charles-Achille[1], Maud Pratlong[4], Alexis Aquilina[4], Eric Trinquet[4], Veronique Perrier[2], Fabien Picaud[3], Joan Torrent[2§], Sebastien Balme[1§*]*

[1] Institut Européen des Membranes, UMR5635 UM ENCSM CNRS, Place Eugène Bataillon, 34095 Montpellier cedex 5, France.

[2] INM UM, CNRS, INSERM, Place Eugène Bataillon, 34095 Montpellier cedex 5, France.

[3] Laboratoire de Nanomédecine, Imagerie et Thérapeutique, EA4662, Université Bourgogne-Franche-Comté (UFR Sciences et Techniques), Centre Hospitalier Universitaire de Besançon, 16 route de Gray, 25030 Besançon, France

[4]PerkinElmer, Parc Marcel Boiteux, 30200 Codolet, France

Extended data 1 : MATERIAL AND METHODS

1. Aβ42 peptide purification and aggregation

Monomer purification. Aβ42 peptides (ERI Amyloid Laboratory LLC, Oxford, CT, USA) were maintained in the monomeric state using the protocol described by Serra-Batiste et al.[1]. Briefly, Aβ42 peptides were dissolved in 6.8 M guanidine thiocyanate solution (Sigma-Aldrich) at a concentration of 8.5 mg mL^{-1}. Then, the solution was sonicated at 52 °C for 5 min, and diluted with ultrapure water (4° C) to reach a final concentration of 5 mg mL^{-1} of Aβ42 peptides and 4 M of guanidine thiocyanate. The solution was centrifuged at 10^5 g at 4° C for 6 min. The collected supernatant was filtered (PVDF, 0.45 µm) and injected into a Superdex 75 Increase 10/300 GL column (GE Heathcare Life Science) previously equilibrated with 10 mM sodium phosphate buffer, pH 7.4. Purification was performed with a 0.5 mL/flow to collect the peak attributed to monomeric Aβ42 (Figure 1a). The Aβ42 peptide concentration was determined with a NanoDrop 8000 spectrophotometer (Thermo Scientific). Peptide aliquots were flash-frozen in liquid nitrogen and stored at -80 °C until use. A similar procedure was followed for Aβ42 peptides labelled with Cy3 (ERI Amyloid Laboratory LLC, Oxford, CT, USA), except that the concentration was determined with a UV spectrophotometer (JASCO). Protein LoBind tubes (Eppendorf) were used for all purification steps.

Preparation and characterization of Aβ42 seeds. Aβ42 stock solution was diluted to 30 µM in 10 mM sodium phosphate buffer, pH 7.4, to reach a final volume of 600 µL in Protein LoBind tubes (Eppendorf). Tubes were arranged vertically and incubated at 25 °C without shaking. Aggregation was monitored with a thioflavin T (ThT) binding assay. Briefly, 20 µL aliquots were withdrawn at specific time points and mixed with 14 µL of 142 mM GlyNaOH buffer, pH 8.3, and 6 µL of 100 µM ThT. Aliquots were then placed in a 96-well plate of black polystyrene with a clear bottom coated with PEG (Thermofisher Scientific). The ThT fluorescence signal of each sample was measured (λ_{ex} = 445 nm and λ_{em} = 485 nm) in a

Fluoroskan Ascent microplate fluorimeter (Thermofisher Scientific). Seeds used for the experiments were harvested after 5 days of incubation.

Transmission electronic microscopy (TEM). Samples of Aβ42 aggregates obtained after 5 days of incubation were deposited onto Formvar carbon-coated grids, negatively stained with freshly filtered 2% uranyl acetate, and dried. TEM images were acquired with a JEOL 1400 electron microscope at an accelerating voltage of 80 kV.

FRET-HTRF experiments. Aβ40 or Aβ42 peptides were left to aggregate in a final volume of 600 µL, in Protein LoBind tubes, at a concentration of 30 µM in 10 mM sodium phosphate buffer at pH 7.4, at 25 °C without agitation. Aliquots were collected at several time points, for ThT fluorescence measurement and HTRF analysis. For ThT fluorescence quantification, 20 µL of each aliquot was mixed with 6 µL of 100 µM ThT solution and 14 µL glycine buffer (pH 8.3). After incubation in a 96-well half area black/clear flat bottom polystyrene plate for 15 min, ThT fluorescence was read at 485 nm with excitation at 444 nm. For HTRF analysis, samples were diluted to 325 ng/mL, flash-frozen in liquid nitrogen, and stored at -80 °C until use. Then, samples were diluted to 0.8 and 20.3 ng/ml (for Aβ40) and to 0.8 and 2.4 ng/ml (for A β1-42). HTRF signals were acquired in triplicate using the HTRF Human Amyloid β1-40 kit (# 62B40PEG) and the HTRF Human Amyloid β1-42 kit (# 62B42PEG) (PerkinElmer, Codolet, France) according to the supplier's recommendations (except some adaptations done for the HTRF Human Amyloid β1-42 kit where the Human Amyloid β 1-42 d2 acceptor antibody was 3-fold diluted and incubation performed at 4° C overnight).

2. Nanopipette pulling and characterization

Quartz capillaries purchased from Sutter Instruments (OD: 1 mm & ID: 0.7 mm) were pulled using a P-2000 pipette puller (Sutter instrument). The pulling parameters used to obtain a tip diameter of 34 nm were: HEAT = 700, FIL = 4, VEL = 60, DEL = 150, PUL = 175. We noticed that the pulling parameters were influenced by several factors, such as the room humidity and

pressure, and also the intrinsic features of the P-2000 instrument, such as laser alignment. Pipettes were filled with pure degassed water following the filling principle described by Sun et al.[2]. After complete filling, nanopipettes were characterized and then coated by addition of L-DOPA solution (8.5 mg/ml) for 2 hours. Then, nanopipettes were carefully washed several times with degassed water to remove excess L-DOPA, and characterized to confirm L-DOPA presence inside the pipettes. The nanopipette geometry was determined by scanning electron microscopy using a Thermo Scientific Quattro ESEM, at high vacuum (10 kV). The contact angle was measured using laboratory-made equipment, and 6 µL deionized water for 10 seconds on the quartz surfaces, before and after L-DOPA coating.

3. RT-FAST assays

For the RT-FAST assays in buffer, Aβ42 monomers were diluted to 100 nM in 1M NaCl/1X PBS, pH = 7.4, and added directly in the pipette without or with seeds (200 pM).

For the RT-FAST assays in CSF, commercially available Cerebrospinal Fluid from Female Cynomolgus Monkey (CUST-BB-28092021-3a, CliniScience) was centrifuged at 4 °C (3000 g) for 3 min, and then spiked with the prepared seeds to obtain a final concentration of 0.2 nM. 16 µl of spiked CSF was added to 384 µl of a solution containing monomers in 1X PBS. The final concentration was 100 nM of monomers and 0.2 nM of seeds in 4 % CSF.

The solutions containing Aβ42 monomers with (experimental condition) or without (control) seeds were placed inside nanopipettes connected to the working electrode of the EPC10 amplifier (HEKA, Lambrecht, Germany) combined with a probe selector (HEKA, Lambrecht, Germany). The ground electrode was placed inside an external reservoir containing 1M NaCl/1X PBS solution. A cycle was composed of two phases. First, a voltage of -500 mV was applied for 10 min and the current was recorded with a sampling rate of 200 kHz filtered with a Bessel filter at 10 kHz. The second step was a 20 min break without voltage. This cycle was repeated for the entire duration of the experiment. The current traces recorded at different

incubation times were analysed using a custom-made Labview software (Peak Nano Tool). Briefly, the signal was filtered with a Butterworth filter of 2 kHz order 1, and then the baseline fluctuations were corrected with a Savitzky-Golay (order 1) filter to determine the detection threshold, here 4 σ (σ is the standard deviation of the baseline signal). Events were characterized by their relative blockade amplitude (ΔI/I) and their time (Δt). Statistical analyses were performed with MATLAB custom scripts (matlab2021a).

4. Aβ (1-42) adsorption on a functionalized quartz substrate.

The adsorption kinetics, fluorescence correlation spectroscopy, and fluorescence lifetime analysis with Aβ (1-42)-Cy3 were performed using a laboratory-made confocal fluorescence setup previously described [3]. Briefly, excitation was ensured with a focused pulsed laser beam SuperK Extreme (NTK Photonics, model EXR-15) combined with superK Varia (NTK Photonics) to select the excitation wavelength at 552 nm. The laser pulse was >10 ps with a repetition rate of 82 MHz. The emitted fluorescence was collected using a HPM-100-40 photodetector (Becker&Hickl) connected to an SPC-130 EM acquisition card (Becker&Hickl). The absence of an after-pulse for this detector allows using a single device to carry out the analysis of the autocorrelation function (see Becker&Hickl). A UPlanaApo 60x/1.20 w objective (Olympus) was used. The confocal volume (approximately 1 fL) and the other calibration coefficients were determined with Alexa-fluor 594 (D=370 μm2 s^{-1}) as standard solution. Aβ42-Cy3 coefficients of diffusion were measured by fluorescence correlation spectroscopy in the bulk solution to confirm that only peptide monomers were used in the adsorption experiments.

The adsorption kinetic of Aβ42-Cy3 (previously purified by FPLC) on a quartz substrate (diameter 25 mm, thickness 120 μm) (NEGS-2, Neyco) coated with L-DOPA, following strictly the same protocol described for the nanopipettes, was deduced from the fluorescence profile. This profile was recorded step by step from the interface of interest to the bulk solution

(at least 50 μm from the interface) by normal scanning (100 nm to 1 μm steps, collection times 50 to 100 ms). From the profile analysis, the amount of adsorbed Aβ42-Cy3 was extracted as previously described. Aβ42-Cy3 fluorescence lifetime was measured in the bulk solution and on the quartz interface. The instrumental response function of the equipment was measured from the reflection at the liquid/quartz interface, and was typically ~130 ps FWHM. The decays were collected at a maximum count rate of 15 kHz into 4096 channels using an SPC-730 acquisition card (Becker & Hickl). The time per channel was set at 6 ps ch^{-1} to fit a full decay in the experimental time window. All decays were collected to have at least 1.5 10^6 counts. Decays were analysed using the Levenberg – Marquardt algorithm, assuming a Poisson distribution of counts in the calculation of the $\chi 2$ criterion. Residual profiles, autocorrelation function, Durbin-Watson test and skewness factor were used to estimate the adjustment quality.

5. Molecular dynamic simulation

All simulations were carried out using the NAMD 2.13 program [4] with the CHARMM36 force field [5] and the TIP3P [6] water model. AD Aβ peptide (1-42) protein structure was obtained from the protein database (ID: 1IYT [7]) and placed in different starting orientations that differed by a rotation/translation around an axis parallel to the surface such as that the lowest protein atom had a distance of 5 to 10 Å from the first surface layer, depending of the simulation.

For all simulations, periodic boundary conditions were used with Particle Mesh Ewald (PME)[8] for long-range electrostatics, a grid spacing of 1.2 Å, and a fourth-order spline interpolation. The system contained ~100k water molecules with 1M NaCl to match the experimental conditions. The system net charge was neutralized for correct PME usage by adding more sodium ions than chloride ions in total. To prevent adsorption on the periodic image of the surface, the system was sufficiently large with a 75 Å thick layer of water between the membrane periodic images. The cut-off for the Van der Waals interactions was set at 12 Å. To build and describe the quartz surface by Lennard-Jones and electrostatic interactions, the

needed parameters were taken from the procedure described in [9] that best fitted the experimental data. Following this protocol, the inner atom positions were heavily constrained to prevent abnormal quartz deformation, while the atoms of the surface were only slightly constrained to better reproduce the quartz-solvent and quartz-L-DOPA interactions.

After energy minimization, all systems were equilibrated at a temperature of 310 K and constant pressure of 1 atm for at least 5 ns with the protein backbone atoms restrained to prevent adsorption before equilibration. Following equilibration, classical molecular dynamic simulations were carried out for 80 ns to 180 ns with a time step of 1.0 fs enabled by the SHAKE [10] algorithm to ensure rigid hydrogen atoms. For all L-DOPA grafting concentrations, two independent simulations were performed with randomized starting velocities and L-DOPA placement on the quartz.

To analyse the simulations, the protein root mean square deviations were extracted during the production phase. Then, during the production phase, pair interactions were extracted from the total duration of the molecular dynamic simulation. These are made of the sum of the Van der Waals and electrostatic contributions between protein and surface/ion/water.

Extended data 2. Scheme of amyloid growth

According to the amyloid cascade hypothesis, Aβ42 self-aggregation leads to the formation of polymorphic structures. It is possible to separate such aggregates into two categories: off-pathway oligomers (i.e. amyloid intermediates that cannot produce fibrils and therefore dissociate into monomers to rearrange) and on-pathway oligomers (i.e. intermediates that can form fibrillar structures). On the other hand, the secondary nucleation process that should enhance Aβ42 aggregation through a seeding mechanism

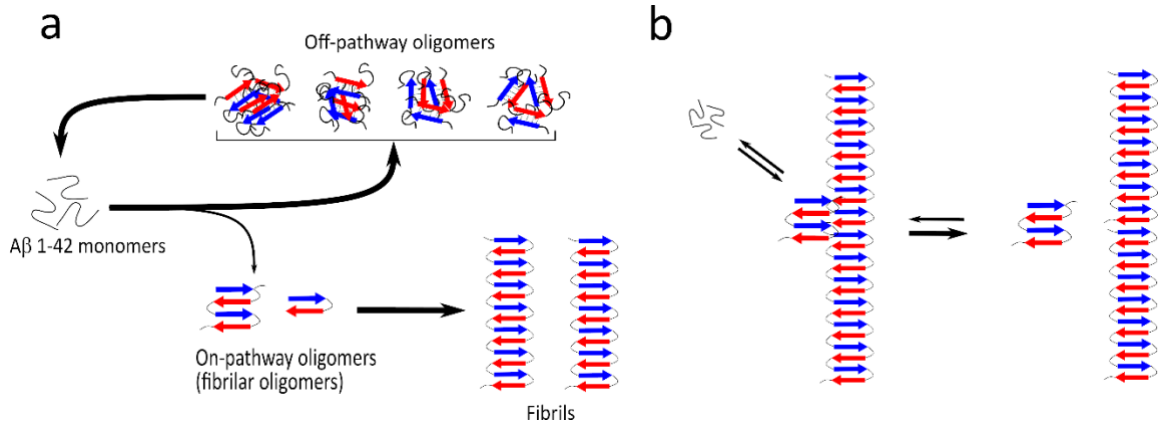

Supplementary Figure 1: a) According to the amyloid cascade hypothesis, Aβ42 self-aggregation leads to the formation of polymorphic structures. It is possible to separate such aggregates into two categories: off-pathway oligomers (i.e. amyloid intermediates that cannot produce fibrils and therefore dissociate into monomers to rearrange) and on-pathway oligomers (i.e. intermediates that can form fibrillar structures). b) Scheme of the secondary nucleation process that should enhance Aβ42 aggregation through a seeding mechanism.

Extended data 2. Characterization of aβ 1-42-Cy3 peptides and Aggregation kinetics

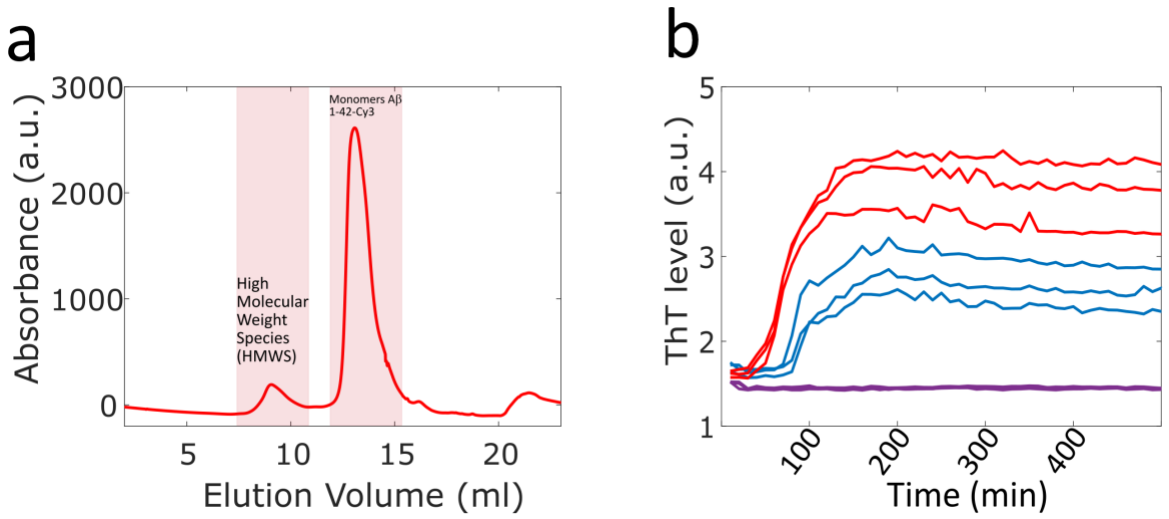

Supplementary Figure 2: a) Size exclusion chromatogram of aβ 1-42-Cy3 peptides after solubilization. Only the peak corresponding to the monomer fraction was harvested, frozen in liquid nitrogen, and stored at -80 °C until the adsorption experiment. b) Aggregation kinetics by ThT by fluorescence monitoring in a plate in the presence or absence of seeds at 37 °C. The monomer concentrations were 4 µM or 100 nM (nanopore condition), and the seed concentrations were 8 nM or 0.2 nM (similar to the nanopore experiments). Experiments were done in triplicate for each condition. These ThT assays showed an increase of ThT fluorescence after 90 min using 100 µl of Aβ42 solution at 4 µM (blue lines). The addition of seeds (8 nM) reduced the time to 50 min (red lines). This highlighted the seeding effect of the preformed seeds used for the RT-FAST experiments. ThT assays performed using the concentration used for RT-FAST (100 nM of Aβ42 and 0.2 nM of preformed seeds) did not show any fluorescence signal enhancement during the 500 min of experiment (violet line). Note that each condition was triplicated.

Extended data 3. Characterisation of Nanopipettes

Supplementary Table 1: Nanopipettes used for all the experiments

Pipette number	G after L-Dopa coating (nS)	Sample
1	3.315	Control Aβ42 monomers only in buffer
2	10.64	Control Aβ42 monomers only in buffer
3	5.116	Control Aβ42 monomers only in buffer
4	2.60	Experimental condition : Aβ42 monomers + Aβ42Seeds (0.2nM) in buffer
5	3.126	Experimental condition : Aβ42 monomers + Aβ42Seeds (0.2nM) in buffer
6		Experimental condition : Aβ42 monomers + Aβ42Seeds (0.2nM) in buffer
7	5.92	Experimental condition : Aβ42 monomers + Aβ42Seeds (0.2nM) in buffer
8	3.748	Experimental condition : Aβ42 monomers + Aβ42Seeds (0.2nM) in buffer
9	7.58	Experimental condition : Aβ42 monomers + Aβ42Seeds (0.2nM) in buffer
10	3.885	Control Aβ42 monomers only in CSF
11	4.398	Control Aβ42 monomers only in CSF
12	5.732	Control Aβ42 monomers only in CSF
13	4.213	Experimental condition : Aβ42 monomers + Aβ42Seeds (0.2nM) in CSF
14		Experimental condition : Aβ42 monomers + Aβ42Seeds (0.2nM) in CSF
15	2.075	Experimental condition : Aβ42 monomers + Aβ42Seeds (0.2nM) in CSF

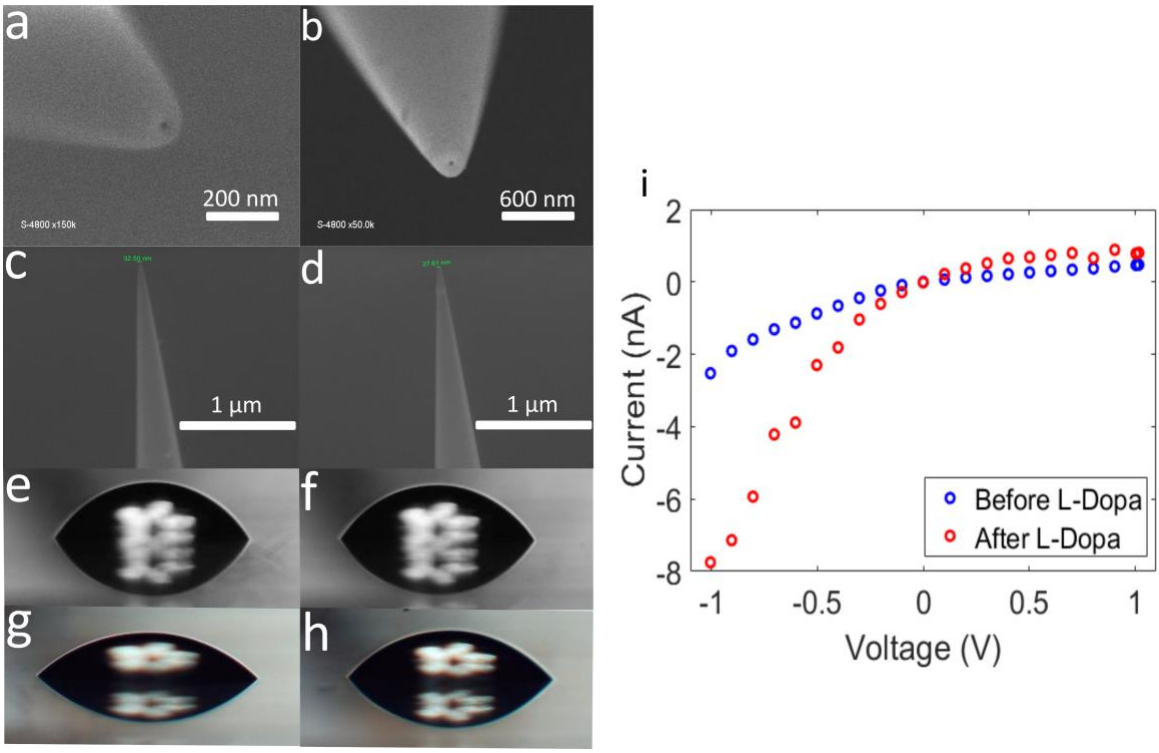

Supplementary Figure 3. a, b, c, d) Scanning electron microscopy images showing the nanopipettes used in the RT-fast experiments. e, f) Contact angles of a water drop on a quartz substrate without L-DOPA coating. The left contact angles are 52.47 and 51.04, the right contact angles are 54.45 and 49.16 for e and f, respectively. g, h) Contact angles of a water drop on a quartz slide with L-DOPA coating. The left contact angles are 36.54 and 44.79, the right contact angles are 37.27 and 39.93 for g and h, respectively. I) Current-Voltage curves before (blue) and after coating with L-DOPA (red) for the nanopipette n. 5.

Extended data 4. Additional results of RT-FAST assay performed in buffer

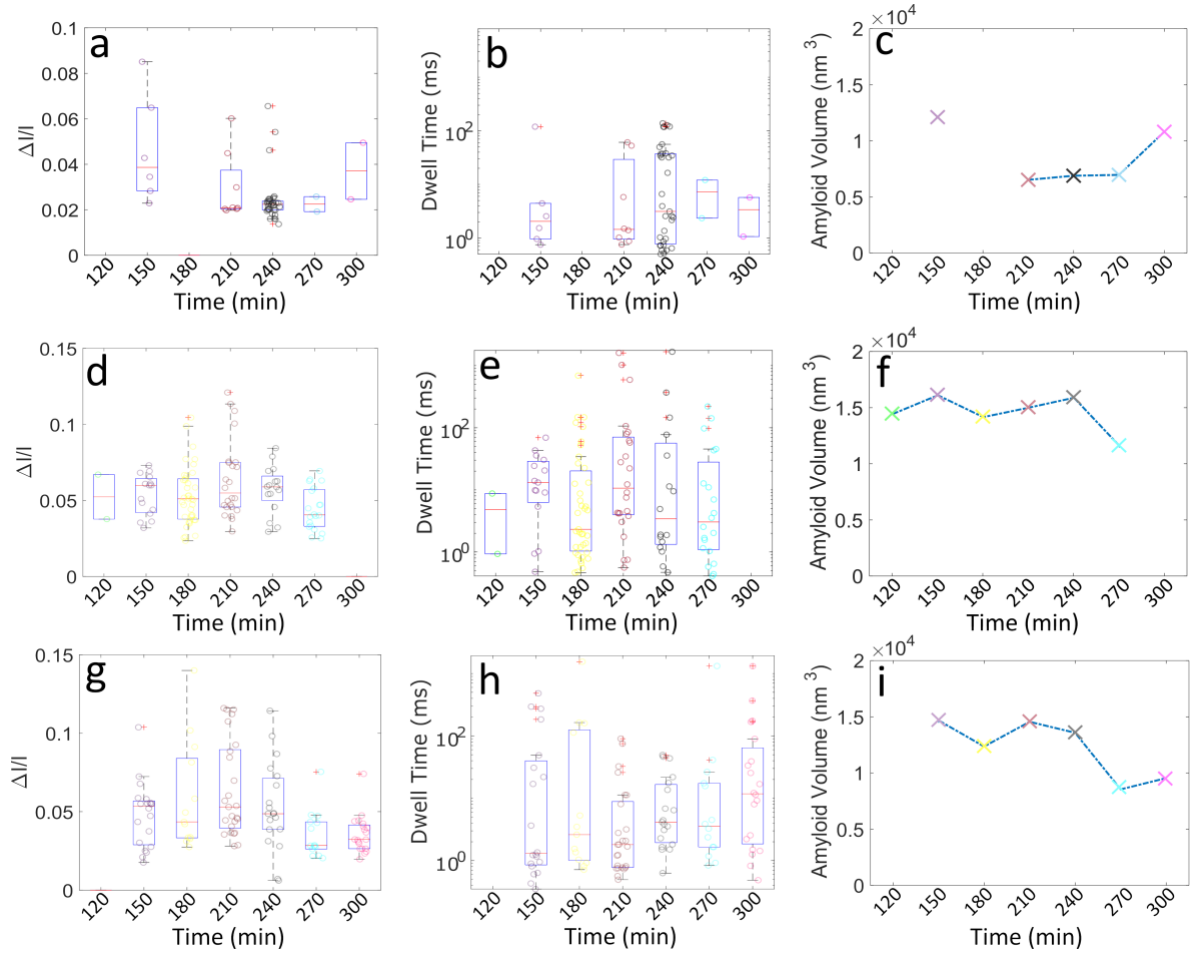

Supplementary Figure 4: a, d, g) ΔI/I of the current blockade obtained with pipettes containing seeds (n. 7,8, and 9 respectively). b, e, h) Dwell time of the current blockade obtained with pipettes containing seeds (n. 7,8, and 9 respectively). c, f, i) Volume of amyloid aggregates passing through the nanopipette estimated with a geometrical model based on the current blockade amplitude (pipette n. 7,8, and 9, respectively).

Extended data 5. Model to determine the amyloid volume

To evaluate the effect of the nanopipette geometry variability (characterized by radius rt, length Lp and a=cos α (see Supplementary Figure 4)), we simulated the expected current blockade amplitude using a previously described geometrical model [11]. (equation 1)

$$\frac{I}{I_0} = 1 - \frac{R_0}{\frac{1}{\kappa\pi}\left[\frac{1}{2ar_{amy}} log\left(\frac{(aL_{amy}+r_t-r_{amy})(r_t+r_{amy})}{(aL_{amy}+r_t+r_{amy})(r_t-r_{amy})}\right)+\frac{L_p-L_{amy}}{(r_t+aL_{amy})r_B}\right]} \quad \text{Eq 1}$$

where R_0 is the open pore resistance and , assuming that amyloids are cylindrical (characterized by length L_{amy} and radius R_{amy} where $L_{amy} = 2r_{amy}$)

We computed the impact of the angle variation on the boundary nanopipette radius previously determined by SEM. A variation of 3° of the angle for a fixed diameter did not represent a large error in the amyloid volume estimation. The diameter was more determinant to estimate the amyloid volume. However, the range of the relative current blockade determined experimentally corresponded to a volume of Aβ aggregates from 490 nm^3 to 1800 nm^3 (supplementary Figure f). These volumes correspond to a sphere with a radius from 5.9 to 9.1 nm. Thus, it is important to note that the given volume in the main manuscript is an order of magnitude and in any case, we do not claim to precisely size each aggregate. Indeed, the relative current amplitude value is influenced by several factors besides the size and geometry of pipette and aggregates, for instance the ionic current rectification, the exact position of the aggregate inside the nanopore, and its orientation.

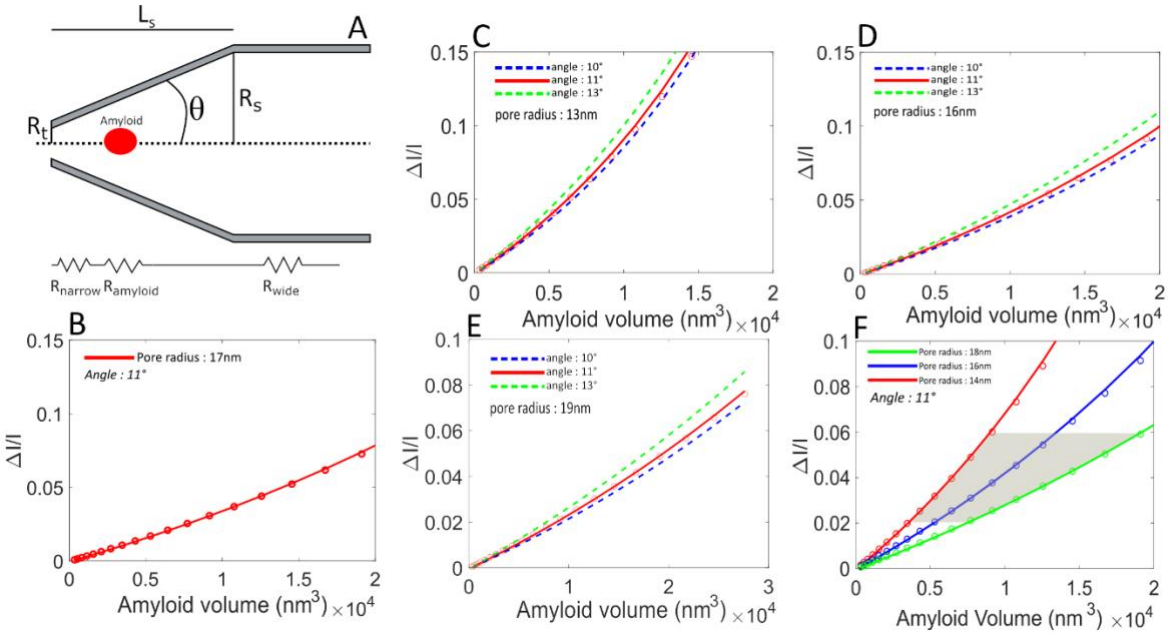

Supplementary Figure 5: a) Sketch representing the geometric parameters of the used nanopipettes. Ls, Rs, Rt correspond to the length of the shank, its radius, and the tip radius, respectively. The angle of the nanopipette cone is represented by θ. b) Graphical resolution of the model to estimate the volumes of amyloid aggregates passing through the pipette based on the blockade amplitude. c, d, e) Graphical resolution of the model to estimate amyloid volumes in function of the blockage amplitudes for different opening angles and pore diameters. f) Graphical resolution for an angle of 11° and different nanopore radius.

Extended data 6. Additional FRET experiments with Aβ40

The aggregation of Aβ42 (Figure 4 k) and Aβ40 (Supplementary Figure 5) in function of time was investigated simultaneously with FRET-HTRF (red curve) and ThT. As the FRET signal is sensitive to the peptide monomeric form, a decrease of the fluorescence signal indicates the formation of Aβ42 (or Aβ40) aggregates. Conversely, ThT fluorescence signal is sensitive to Aβ42 (or Aβ40) aggregates that adopt a β-sheet structure. The combination of the two assays allows deducing the transient species formed during the lag phase. We observed oscillations in the FRET signal (especially at the lowest concentration: 0.8 ng/ml), probably indicating the formation and the dissociation of aggregate species during the early aggregation phases. These aggregates are not included in the β-sheet structure because the ThT signal remained constant. Subsequently, once the exponential phase of aggregation started (increasing ThT signal), the FRET-HTRF signal decreased indicating the formation of amyloid fibrils. Finally, when the plateau phase was reached (stabilization of the ThT signal), the FRET-HTRF signal was very low, indicating the consumption of monomer species.

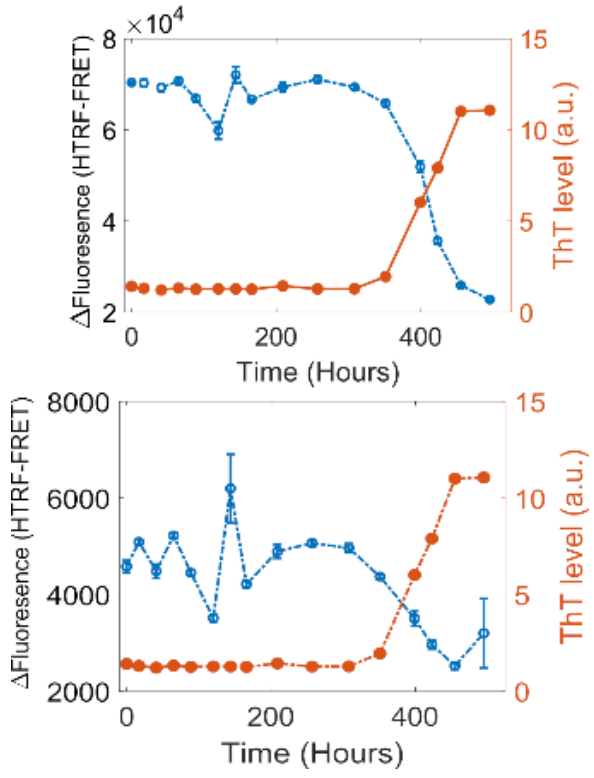

Supplementary Figure 6: Aggregation kinetics of Aβ40 peptide by ThT fluorescence monitoring (red curve). The HTRF-FRET fluorescence signal shows oscillations of species during the early phases of aggregation (blue curve) at two concentrations: 20.3 ng/ml (top) and 0.8 ng/ml (bottom).

Extended data 7. Aβ adsorption kinetics

The adsorption kinetic (k_{ads}) of the Aβ(42)-Cy3 monomer was experimentally determined from the time-resolved measurement of the interfacial concentration using a confocal spectrometer.

$$n_{Sol,A\beta(42)} \underset{\Leftrightarrow}{k_{ads}} n_{ads,A\beta(42)}$$

where $n_{Sol,A\beta(42)}$ and $n_{ads,A\beta(42)}$ are the number of Aβ42 monomers in solution and adsorbed on the quartz surface, respectively. They were calculated from the experimental measurement of the interfacial concentration of Aβ(42) ($\Gamma_{A\beta42}$) at the equilibrium (Supplementary Figure 6) and the substrate surface. At the equilibrium, the adsorption constant can be deduced from the following equation.

$$k_{ads} = \frac{n_{ads,A\beta(42)}}{n_{Sol,A\beta(42)}}$$

As the fluorescence lifetime of Aβ(42)-Cy3 in bulk and adsorbed on the surface were similar, no correction of the quantum yield variations due to the substrate/fluorophore interactions was required.

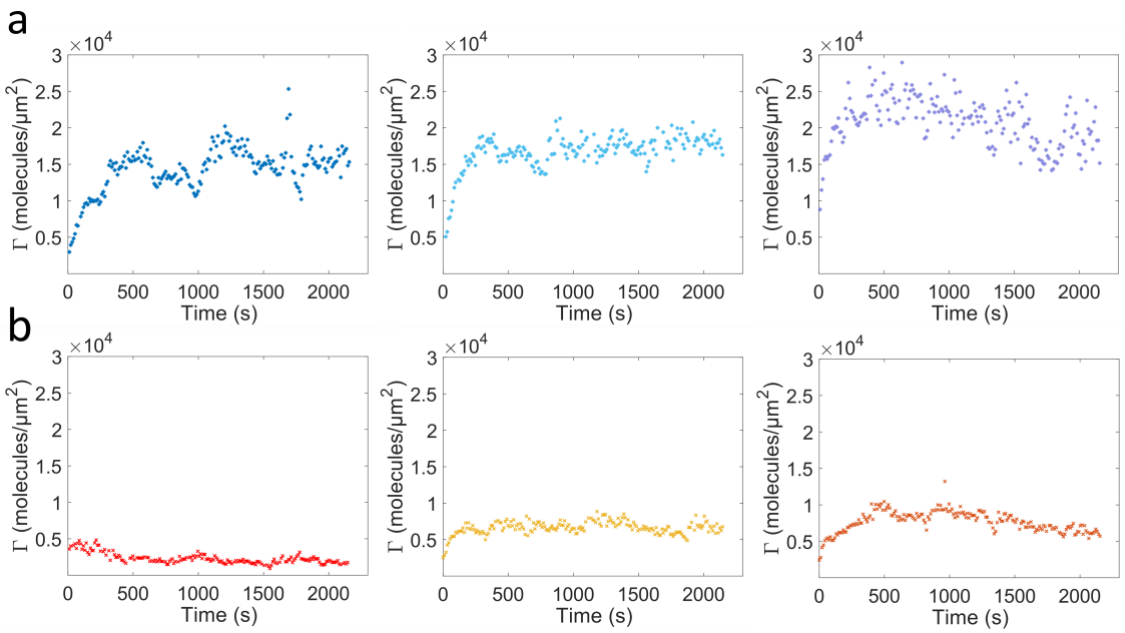

Supplementary Figure 7: a) Change in the number of Aβ 1-42-Cy3 monomers per µm² over time (n=3 different experiments in buffer without CSF). b) Change in the number of Aβ 1-42 monomers per µm² over time (n= 3 different experiments with 4% CSF).

Extended data 8. Molecular dynamic simulations

In Supplementary Figure 7, the pair interactions between Aβ42 and the different molecules in the reservoir were plotted (different L-DOPA concentrations). During the simulation, Aβ42 oscillates from the adsorbed to the desorbed state on the quartz surface. Aβ42 interaction with water molecules significantly oscillates, in competition with the other contributions, indicating that these molecules can play an important role in the monomer behaviour. Due to the presence of organized water shells on the surface, the monomer interaction is destabilized at the approach of the quartz surface in the absence of L-DOPA coating.

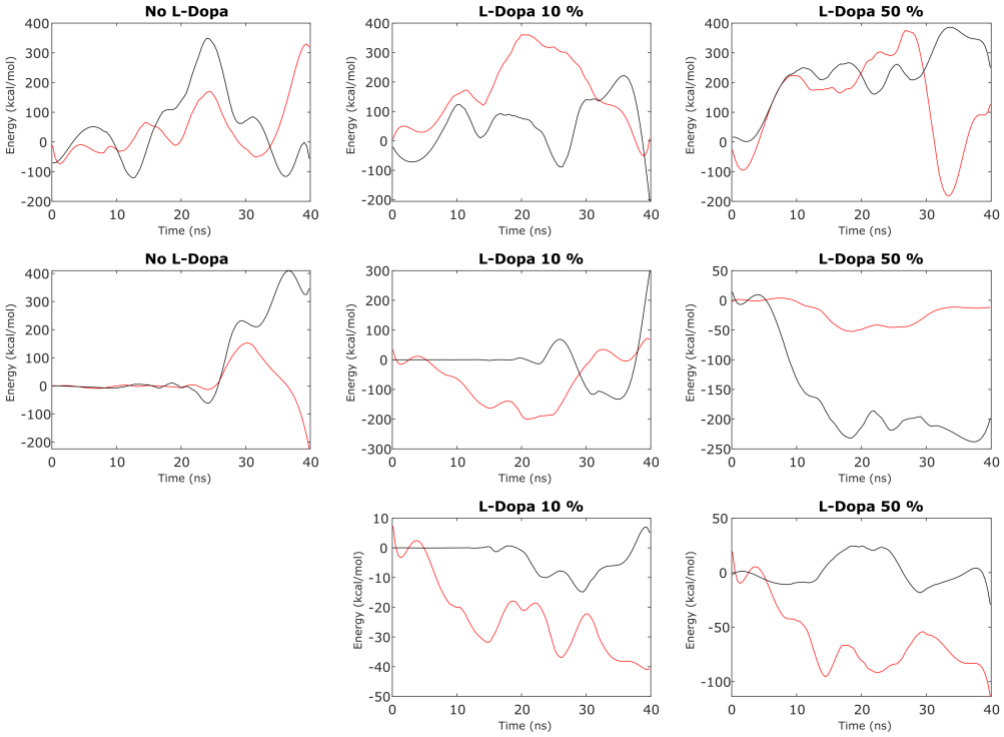

Supplementary Figure 8: Pair interactions between Aβ42 and water: (a) with non-functionalized SiO2; (b) with SiO2 functionalized with 10% L-DOPA; (c) with SiO2 functionalized with 50% L-DOPA. Black and red curves are for two different simulation conditions.

Precisely, Aβ42 interacts with the quartz surface (+ organized water shells) through specific interactions with its residues. Depending on the Aβ42 orientation, residues can be well oriented or not. This perturbs the adsorption phenomena and limits the contact between Aβ42 and the surface. This selective adsorption of residues onto quartz and the thermal agitation alter the strength of the interactions between the monomer and the surface. Therefore, the signal oscillates and changes during the simulation, allowing the monomer to be trapped for a certain duration before returning to the bulk reservoir and coming back to the surface. The increase of L-DOPA concentration modifies the solvent at the direct proximity of the surface and favours

slightly the monomer adsorption because of the modification of the water shell organization at the quartz surface.

To explain the modification of the water shell organization at the quartz surface, we plotted in Supplementary Figure 8, the coordination number of water with the quartz surface, obtained after the integration of the radial distribution function of water around the surface. These coordination numbers showed a slight decrease of the water neighbouring around the quartz surface depending on the L-DOPA concentration that could explain the monomer adsorption behaviour change.

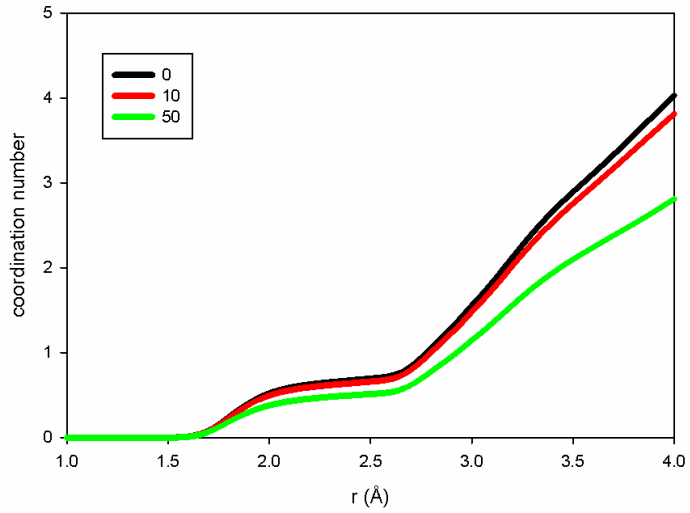

Supplementary Figure 9: Coordination number of water with the SiO_2 surface in function of the L-DOPA concentration (black: 0%; red: 10%; green: 50%).

Extended data 10. Comparison of RT-fast experiment without and with 4% CSF

The median frequencies and the centre of current blockade amplitude were taken between 120 and 300 minutes of aggregation for the control condition (without CSF; blue) and between 240 and 420 minutes of aggregation for the experimental condition (with CSF; red)

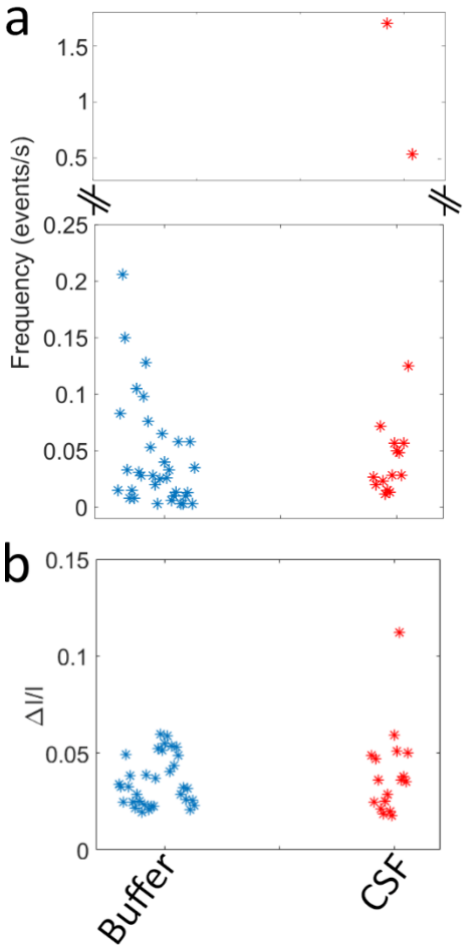

Supplementary Figure 10: Comparison of the current blockade a) frequencies and b) amplitude in the experiments without (blue) and with 4% CSF (red).

References

(1) Serra-Batiste, M.; Ninot-Pedrosa, M.; Bayoumi, M.; Gairí, M.; Maglia, G.; Carulla, N. *Proceedings of the National Academy of Sciences of the United States of America* **2016**, DOI: 10.1073/pnas.1605104113.

(2) Sun, L.; Shigyou, K.; Ando, T.; Watanabe, S. *ANALYTICAL CHEMISTRY* **2019**, DOI: 10.1021/acs.analchem.9b03848.

(3) Balme, S.; Coulon, P. E.; Lepoitevin, M.; Charlot, B.; Yandrapalli, N.; Favard, C.; Muriaux, D.; Bechelany, M.; Janot, J.-M. *Langmuir : the ACS journal of surfaces and colloids* **2016**, DOI: 10.1021/acs.langmuir.6b02048.

(4) Phillips, J. C.; Braun, R.; Wang, W.; Gumbart, J.; Tajkhorshid, E.; Villa, E.; Chipot, C.; Skeel, R. D.; Kalé, L.; Schulten, K. *Journal of computational chemistry* **2005**, DOI: 10.1002/jcc.20289.

(5) MacKerell, A. D.; Bashford, D.; Bellott, M.; Dunbrack, R. L.; Evanseck, J. D.; Field, M. J.; Fischer, S.; Gao, J.; Guo, H.; Ha, S.; Joseph-McCarthy, D.; Kuchnir, L.; Kuczera, K.; Lau, F. T.; Mattos, C.; Michnick, S.; Ngo, T.; Nguyen, D. T.; Prodhom, B.; Reiher, W. E.; Roux, B.; Schlenkrich, M.; Smith, J. C.; Stote, R.; Straub, J.; Watanabe, M.; Wiórkiewicz-Kuczera, J.; Yin, D.; Karplus, M. *The journal of physical chemistry. B* **1998**, DOI: 10.1021/jp973084f.

(6) Jorgensen, W. L.; Chandrasekhar, J.; Madura, J. D.; Impey, R. W.; Klein, M. L. *The Journal of chemical physics* **1983**, DOI: 10.1063/1.445869.

(7) Scheufler, C.; Sebald, W.; Hülsmeyer, M. *Journal of Molecular Biology* **1999**, DOI: 10.1006/jmbi.1999.2590.

(8) Darden, T.; York, D.; Pedersen, L. *The Journal of chemical physics* **1993**, DOI: 10.1063/1.464397.

(9) Comer, J. R.; Wells, D. B.; Aksimentiev, A. *Methods in molecular biology (Clifton, N.J.)* **2011**, DOI: 10.1007/978-1-61779-142-0_22.

(10) Ryckaert, J.-P.; Ciccotti, G.; Berendsen, H. J. *Journal of Computational Physics* **1977**, DOI: 10.1016/0021-9991(77)90098-5.

(11) Giamblanco, N.; Coglitore, D.; Gubbiotti, A.; Ma, T.; Balanzat, E.; Janot, J.-M.; Chinappi, M.; Balme, S. *ANALYTICAL CHEMISTRY* **2018**, DOI: 10.1021/acs.analchem.8b03523.